FERMILAB-TM-2400-APC

Investigation of the Helical Cooling Channel (analysis, tracking, simulation)

V.Balbekov

Fermi National Accelerator Laboratory

P.O. Box 500, Batavia, Illinois 60510

December 20, 2007

Abstract

Derbenev's helical cooling channel is investigated by comparison of analytical and numerical results including particle tracking and cooling simulation. Optimization of the channel and estimation of its ultimate potentiality are presented as well.

1 Introduction

Helical channel for ionization cooling of muons is proposed by Y. Derbenev [1] and most minutely presented in Ref. [2]. Cooling simulation performed by K.Yonehara et al. confirms the idea on the whole [3, 4]. However, detailed analysis and comparison of analytical and numerical results are not developed yet. This is an important issue because the theoretical analysis is based essentially on paraxial approximation and therefore has restricted areas of application. This is main objective of presented work including estimation of ultimate properties of the channel and its optimization with help of analytical methods, particle tracking and cooling simulation.

A compendium of some related formulae is given in Sec. 2. Most of them coincide with similar expressions in [2], though partly different method and notation are used to provide more convenience of comparison with numerical results.

Particle tracking and cooling simulation are presented in next sections. It is assumed that the cooling is provided by ionization energy loss in a gas of constant density which fills the channel. Investigation of betatron motion is the main objective of Sec. 3–6 where the simplest accelerating field is applied ("inductive regime"). RF regime is shortly considered in Sec. 7 demonstrating significant degradation of the cooler parameters. The results are summarized in the Conclusion.

2 Some analytical formulae

Some general formulae are collected in this section in a convenient form to use them for subsequent analysis and comparison with tracking/simulation results. Most of them were obtained first in Ref. [1, 2].

2.1 Magnetic field and equations of motion

Components of the helical magnetic field in cylindrical frame z-r-θ are [2]:

$$B_z = -\sum_{n=1}^{\infty} B_n I_n(n\kappa r)\,\cos n(\theta-\kappa z) - B_0, \tag{1}$$

$$B_r = \sum_{n=1}^{\infty} B_n I_n'(n\kappa r)\,\sin n(\theta-\kappa z), \tag{2}$$

$$B_\theta = \frac{1}{\kappa r}\sum_{n=1}^{\infty} B_n I_n(n\kappa r)\,\cos n(\theta-\kappa z) \tag{3}$$

where $I_n(X)$ is modified Bessel function of n-th order [1], B_n are arbitrary coefficients, and $2\pi/\kappa$ is the helix period. Using z as an independent variable, one can write equations of motion in the form:

$$\frac{d}{dz}\left(\frac{v_z dr}{dz}\right) = \frac{e}{m\gamma c}\left(rB_z\frac{d\theta}{dz} - B_\theta\right) + rv_z\left(\frac{d\theta}{dz}\right)^2, \tag{4}$$

$$\frac{d}{dz}\left(\frac{v_z r d\theta}{dz}\right) = \frac{e}{m\gamma c}\left(B_r - B_z\frac{dr}{dz}\right) - v_z\frac{dr}{dz}\frac{d\theta}{dz} \tag{5}$$

[1] Only first kind functions are used in Ref. [1, 2] and in this paper. However, second kind functions are acceptable also if the channel does not include line $r = 0$ being separated by a coil.

where γ is normalized energy. Relation of longitudinal velocity v_z to total velocity v will be used as 3rd equation:

$$\frac{v_z}{v} = \frac{dz}{vdt} = \left[1 + \left(\frac{dr}{dz}\right)^2 + \left(\frac{rd\theta}{dz}\right)^2\right]^{-1/2}. \tag{6}$$

At motion in magnetic field, v and γ are invariable. Equation for energy will be added later to take into account ionization energy loss and compensating accelerating field.

2.2 Equilibrium helical trajectories

Series (1)–(6) has partial solutions which will be referred further as equilibrium ones:

$$r = R = X/\kappa = const, \qquad \theta = \kappa z \tag{7}$$

where the helix parameter X depends on momentum $p = m\gamma v$ and satisfies the equation:

$$\left(1 + F(X)\,\frac{1+X^2}{X^2}\right)\sqrt{1+X^2} = \frac{\kappa pc}{eB_0}\,. \tag{8}$$

Used function F is the most important characteristic of the helical field:

$$F(X) = \frac{1}{B_0}\sum_{n=1}^{\infty} B_n I_n(nX)\,. \tag{9}$$

Note that $-B_0[\,1 + F(X)\,]$ is z component of the field on equilibrium trajectory of radius $R = X/\kappa$.

2.3 Reference orbit and dispersion

Resolving Eq. (8), one can find dependence $X(p) = \kappa R(p)$ that is dispersion. The equilibrium trajectory of momentum p_0 is used below as a reference one. Corresponding dispersion function $D = p_0 R'(p_0)$ can be presented in the form:

$$\kappa D = \frac{[\,1 + X_0^2\,]\,[\,2 - G(X_0)\,]}{X_0\,[\,2 - G(X_0)\,] + [\,1 + X_0^2\,]\,G'(X_0)} \tag{10}$$

where

$$G(X) = \frac{X^2 + 2(1+X^2)F(X)}{X^2 + (1+X^2)F(X)}\,. \tag{11}$$

It will be shown soon that this function is actually the coupling parameter of betatron oscillations. With help of this function, Eq. (8) obtains the form:

$$\frac{\sqrt{1+X^2}}{2-G(X)} = \frac{\kappa pc}{eB_0}\,.$$

2.4 Small oscillations

We represent general solution of series (1)–(6) in the form:

$$r = R_0 + \rho\,, \qquad \theta = \kappa z + \frac{\kappa\xi\sqrt{1+X_0^2}}{X_0}\,. \tag{12}$$

where new variables ρ and ξ are normal deviations from the reference orbit. In linear approximation, they satisfy the equations:

$$\frac{d^2\rho}{dz^2} + Q_\rho^2\kappa^2\rho = \frac{\kappa G(X_0)}{\sqrt{1+X_0^2}}\,\frac{d\xi}{dz} + \kappa^2 R_0\,\frac{\Delta p}{p}\,, \tag{13}$$

$$\frac{d^2\xi}{dz^2} + Q_\xi^2\kappa^2\xi = -\frac{\kappa G(X_0)}{\sqrt{1+X_0^2}}\,\frac{d\rho}{dz} \tag{14}$$

where $\Delta p/p = (p–p_0)/p_0$ is relative momentum deviation, and the tunes are:

$$Q_\rho^2 = \frac{X_0^2}{1+X_0^2} + \frac{X_0G'(X_0)}{2-G(X_0)}, \qquad Q_\xi^2 = \frac{2\,[\,1-G(X_0)\,]}{1+X_0^2} - \frac{X_0G'(X_0)}{2-G(X_0)} \tag{15}$$

Note the relation $D = R_0/Q_\rho^2$ which is inherent also in symmetric ring accelerators. Subindex '0' will be omitted below: $X = X_0$, $G = G(X_0)$, etc.

2.5 Eigenmodes and eigentunes

General solution of system (13)–(14) is:

$$\rho = A_1\cos\psi_1 + \alpha_2 A_2\sin\psi_2, \qquad \xi = \alpha_1 A_1\sin\psi_1 + A_2\cos\psi_2 \tag{16}$$

where $\psi_{1,2} = \kappa\nu_{1,2}z + \phi_{1,2}$, A and ϕ are arbitrary constants. Eigentunes ν and coefficients α have to be found from the relations:

$$\nu_{1,2}^2 = \frac{1}{2}\left(Q_\rho^2 + Q_\xi^2 + \frac{G^2}{1+X^2}\right) \mp \frac{1}{2}\sqrt{\left(Q_\rho^2 + Q_\xi^2 + \frac{G^2}{1+X^2}\right)^2 - 4Q_\rho^2Q_\xi^2} \tag{17}$$

$$\alpha_{1,2}^2 = \frac{\nu_{1,2}^2 - Q_\rho^2}{\nu_{1,2}^2 - Q_\xi^2}\,. \tag{18}$$

Geometrically, the eigenmodes are elliptical helixes around the reference trajectory with relation of axis $\xi/\rho = \alpha_1$ for 1st mode and $\rho/\xi = \alpha_2$ for 2nd one. We will choose sign in Eq. (17) to get $\nu_1^2 < \nu_2^2$ at $Q_\rho^2 < Q_\xi^2$ and vice versa. Then $\alpha_{1,2}^2 < 1$, and $A_{1,2}$ are simply maximal deviations from the reference line.

2.6 Integrals of motion

Squares of the amplitudes $A_{1,2}$ in Eq. (16) are integrals of motion. For future convenience, we represent them in the form $A_i^2 = C_i^2 + S_i^2$ where

$$C_1 = \frac{\nu_2\rho + \alpha_2\xi_z'/\kappa}{\nu_2 + \alpha_1\alpha_2\nu_1}\,, \qquad S_1 = \frac{\rho_z'/\kappa - \alpha_2\nu_2\xi}{\nu_1 + \alpha_1\alpha_2\nu_2}\,, \tag{19}$$

$$C_2 = \frac{\nu_1\xi + \alpha_1\rho_z'/\kappa}{\nu_1 + \alpha_1\alpha_2\nu_2}\,, \qquad S_2 = \frac{\xi_z'/\kappa - \alpha_1\nu_1\rho}{\nu_2 + \alpha_1\alpha_2\nu_1}\,, \tag{20}$$

and $\xi_z' = d\xi/dz$, etc. In these terms, 4D rms emittance of the beam in space of transverse coordinates – normalized momenta is:

$$\varepsilon_{\rho,p_\rho,\xi,p_\xi} = \varepsilon_1\varepsilon_2, \qquad \varepsilon_1 = \beta\gamma\frac{A_1^2}{\hat\beta_1}, \qquad \varepsilon_2 = \beta\gamma\frac{A_2^2}{\hat\beta_2} \tag{21}$$

where $\beta = v/c$ is normalized beam velocity, and $\hat\beta$ can be treated as beta-functions:

$$\hat\beta_1 = \frac{\sqrt{1+X^2}}{\kappa(\nu_1 + \alpha_1\alpha_2\nu_2)}, \qquad \hat\beta_2 = \frac{\sqrt{1+X^2}}{\kappa(\nu_2 + \alpha_1\alpha_2\nu_1)}\,. \tag{22}$$

2.7 Cooling decrements

Beam cooling provided by ionization energy loss in a gas of constant density which fills the channel is considered in this work. Without stochastic processes, this produces additional force:

$$\vec F_i = -\frac{E_i(p)\,\vec p}{p} \tag{23}$$

where E_i is ionization energy loss per unit length. For reference particle, this force should be compensated by accelerating field. The simplest field which has required properties and satisfies Maxwell equations is: [2]

$$\vec{F}_a = \frac{E_i(p_0)\,\vec{a}}{\sqrt{1+X^2}}, \qquad (a_z,\ a_r,\ a_\theta) = \left(1,\ 0,\ \frac{XR}{r}\right). \tag{24}$$

It will be used firstly for investigation of transverse cooling. Peculiarities of FR cooling are shortly discussed in Sec. 7.

At assumptions (23)–(24), linearized equation for energy of a particle is:

$$\frac{d\Delta E}{dz} = -\sqrt{1+X^2}\,\frac{dE_i}{dE}\,\Delta E - \frac{E_i X\kappa\rho}{\sqrt{1+X^2}} \tag{25}$$

where $\Delta E = E - E_0 = \beta^2 E\Delta p/p$ is deviation of the energy from central value. The additional force in Eq. (4)–(5) does not effect on the reference trajectory, but changes equations of small betatron oscillations (13)–(14) which turn to

$$\frac{d^2\rho}{dz^2} + Q_\rho^2\kappa^2\rho = \frac{\kappa G}{\sqrt{1+X^2}}\,\frac{d\xi}{dz} - \frac{E_i\sqrt{1+X^2}}{\beta^2 E}\,\frac{d\rho}{dz} + \frac{\kappa^2 R\,\Delta E}{\beta^2 E}\,, \tag{26}$$

$$\frac{d^2\xi}{dz^2} + Q_\xi^2\kappa^2\xi = -\frac{\kappa G}{\sqrt{1+X^2}}\,\frac{d\rho}{dz} - \frac{E_i\sqrt{1+X^2}}{\beta^2 E}\,\frac{d\xi}{dz} - \frac{2E_i\kappa\rho}{\beta^2 E} - \frac{dE_i}{dE}\frac{X\Delta E}{\beta^2 E} \tag{27}$$

The cooling results in a damping of transverse amplitudes and energy deviation, a process which we present in the form:

$$A_{1,2}^2 \text{ and } \Delta E \quad \propto \quad \exp\left(-\frac{E_i\lambda s}{\beta^2 E}\right) = \exp\left(-\frac{E_i\lambda\sqrt{1+X^2}\,z}{\beta^2 E}\right) \tag{28}$$

where $s = z\sqrt{1+X^2}$ is the way measured along the reference trajectory, and the factors λ are partial normalized decrements. Their sum can be found with help of Jacoby theorem, and substitution $\rho = D\Delta p/p$ in Eq. (25) allows to separate energy decrement resulting in

$$\lambda_1 + \lambda_2 + \lambda_E = 2 + \beta^2\frac{d\ln E_i}{d\ln E}\,, \qquad \lambda_E = \frac{XD\kappa}{1+X^2} + \beta^2\,\frac{d\ln E_i}{d\ln E}\,. \tag{29}$$

[2]The field can be realized as a combination of inductive azimuthal component and inductive or electrostatic longitudinal one. Therefore, further we will treat it as an "inductive" field.

The approximation

$$E_i \propto \frac{1}{\beta^2} \tag{30}$$

is acceptable in many cases because coefficient of proportionality depends on momentum enough weakly to use its central value in practice. Then equations (29) give:

$$\lambda_1 + \lambda_2 + \lambda_E = 2\beta^2\,, \qquad \lambda_E = \frac{XD\kappa}{1+X^2} - \frac{2}{\gamma^2}\,. \tag{31}$$

All the decrements could be found by substitution of a solution $\propto \exp\,(i\kappa\nu z)$ in series (25)–(27) and by solution of obtained dispersion equation. This is simply in principle but general formula is extremely cumbersome. Therefore, only concerned particular results will be presented in next sections.

2.8 Equilibrium emittances

With both the ionization cooling and multiple Coulomb scattering taken into account, equilibrium rms amplitudes are:

$$\langle A_{1,2}^2\rangle_{eq} = \frac{C_{sct}}{2\gamma\lambda_{1,2}}\,(\hat\beta_{1,2}^2 + \alpha_{2,1}^2\hat\beta_{2,1}^2), \qquad C_{sct} = \frac{1}{mE_i}\frac{d\langle p_\perp^2\rangle}{ds} \tag{32}$$

where m is muon mass, $d\langle p_\perp^2\rangle/ds$ is rms momentum of scattering in any transverse direction per unit of path . Using Eq. (21), one can find equilibrium emittances:

$$(\varepsilon_1)_{eq} = \frac{\beta C_{sct}(\hat\beta_1^2 + \alpha_2^2\hat\beta_2^2)}{2\lambda_1\hat\beta_1}, \qquad (\varepsilon_2)_{eq} = \frac{\beta C_{sct}(\hat\beta_2^2 + \alpha_2^2\hat\beta_2^2)}{2\lambda_2\hat\beta_2} \tag{33}$$

Equilibrium rms energy spread is conditioned by longitudinal cooling and straggling, and can be presented in the form:

$$(\sigma_E)_{eq}^2 = \frac{E^2\beta^4(\gamma^2+1)}{2\lambda_E\gamma}\,C_{str}\,, \qquad C_{str} = \frac{1}{mc^2E_i\beta^2(\gamma^2+1)}\,\frac{d\langle E^2\rangle}{ds}\,. \tag{34}$$

Besides of this, straggling and dispersion bring some additions to the transverse emittances:

$$(\Delta\varepsilon_1)_{eq} = \frac{\beta(\gamma^2+1)\nu_2^2\hat\beta_2^2\kappa^2D^2C_{str}}{2\lambda_1\hat\beta_1(1+X^2)}\,, \qquad (\Delta\varepsilon_2)_{eq} = \frac{\beta(\gamma^2+1)\nu_1^2\alpha_1^2\hat\beta_2\kappa^2D^2C_{str}}{2\lambda_2(1+X^2)}\,. \tag{35}$$

Note that parameters C_{sct} and C_{str} depend only slightly on momentum like coefficient of proportionality in Eq. (30). Further we will apply the values:

$$C_{sct} = 6.9 \times 10^{-3}, \qquad C_{str} = 2.0 \times 10^{-4}$$

which inhere in hydrogen at momentum 250 MeV/c. Note that general variables r, θ and corresponding momenta p_r, p_θ are used in the computer code. Relations of the coordinates are given by Eq. (12), and corresponding relations for the momentum components are:

$$\frac{p}{\sqrt{1+X^2}}\frac{d\rho}{dz} = p_\rho = p_r, \quad \frac{p}{\sqrt{1+X^2}}\frac{d\xi}{dz} = p_\xi = p_\theta\sqrt{1+X^2} - pX - \frac{p\rho\kappa}{1+X^2} \tag{36}$$

3 HCC without linear coupling

The nearest goal is a comparison and mutual checking of analytical and numerical results. Globally uncoupled system $G(X) \equiv 0$ would be the most convenient for this. However, it follows from Eq. (10) and (31) that $\lambda_\rho = 0$ at any X in this case, a fact which makes impossible full analysis of the cooling. Therefore, we consider in this section a locally uncoupled system with reference radius $X_0 = 1$ and parameters

$$G(1) = 0, \quad G'(1) = 0.9, \quad p = 264 \text{ MeV}, \quad \kappa = 2\pi/\text{m}, \quad E_i = 17.3 \text{ MeV/m}$$

Then the main solenoid field $B_0 = 5.53$ T. The formulae of previous section are applicable in this case at $\nu_1 = Q_\rho = 0.975$, $\nu_2 = Q_\xi = 0.742$, $\alpha_{1,2} = 0$.

3.1 Field composition

According to Eq. (9) and (11), function $F(X)$ should be composed from Bessel functions to provide $F(1) = -0.25$, $F'(1) = -0.1375$. Minimal set includes 2 terms:

$$B_1/B_0 = -0.680, \qquad B_2/B_0 = 0.195$$

providing the field which is plotted in Fig. 1 by red line. However, it turned out that dynamic aperture of this channel is rather small being comparable with equilibrium beam size. Because of this, a noticeable particles loss

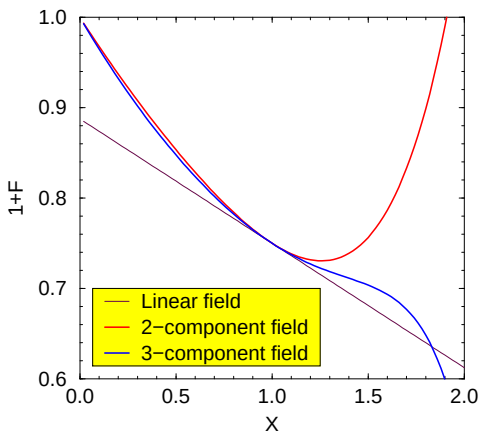

Figure 1: Two- and three-component longitudinal field on the reference trajectory. Linear field $1+F = 0.75 - 0.1375(X-1)$ is shown for comparison.

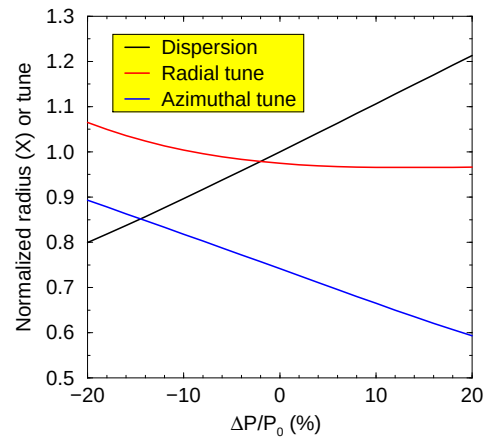

Figure 2: Dispersion and tunes vs relative particle momentum at 3-component field. High precision tracking, distinction from theory is less of 1×10^{-6} at $\Delta p/p = 0$.

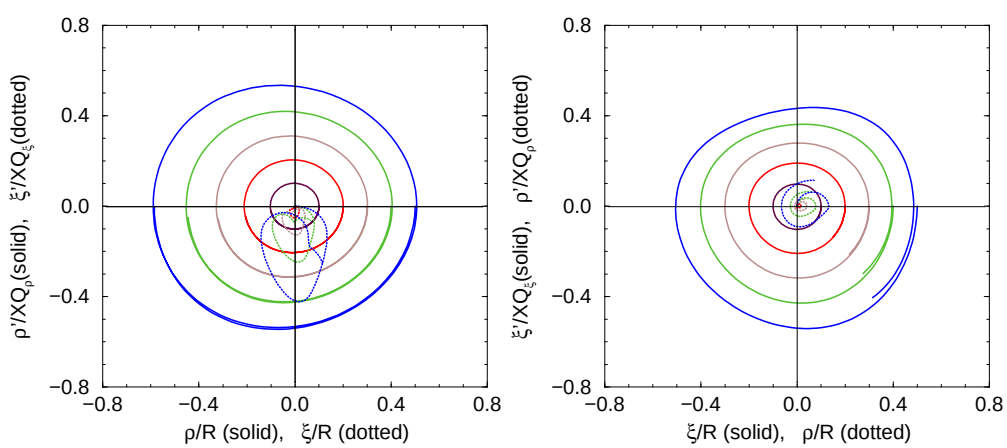

Figure 3: Phase trajectories of transverse motion. Initial particle deviation is taken in radius (left) or in azimuth (right), and corresponding trajectories are plotted by solid lines. Attendant projections on another plane are plotted by thin dotted lines of the same color.

appears at the cooling simulation, hampering the analysis. Therefore, more promoted 3-component field is taken for the investigation

$$B_1/B_0 = -0.733, \qquad B_2/B_0 = 0.294, \qquad B_2/B_0 = -0.040$$

providing blue line field in Fig. 1. [3]

3.2 Dispersion and chromaticity

Normalized dispersion and tunes vs $\Delta p/p$ are plotted in Fig. 2. Dispersion is found by solution of Eq. 8 with 3-component composed field. Tracking with step 5 μm at betatron amplitude 0.1 mm is used to determine the tunes. At $\Delta p/p = 0$ analytical and numerical results differ not more of 10^{-6}. Step 100 μm is used at cooling simulation providing tracking accuracy $\sim 10^{-4}$.

3.3 Phase trajectories

Phase trajectories are plotted in Fig. 3 at central particle momentum. The variables $\rho' = d\rho/dz$, etc. defined according to Eq. (36) are used in the graphs. At small amplitude, the trajectories are circles at this scale. This fact is in a full agreement with Eq. (22) for beta-functions, resulting numerically: $\beta_\rho = 23.1$ cm and $\beta_\xi = 30.4$ cm. Distortions at large amplitudes let us to estimate dynamic aperture of the channel aperture as $0.4/\kappa \sim 7$ cm. Note that without sextupole correction it is almost 2 times less.

3.4 Cooling decrements

Eq. (31) predicts the normalized cooling decrements:

$$\lambda_\rho = 0.474, \qquad \lambda_\xi = 1, \qquad \lambda_E = 0.250\,.$$

At accepted ionization energy loss, corresponding cooling lengths Δz are 21.1 m, 10.0 m, and 40.0 m. This is confirmed by single particle tracking shown in Fig. 4. Solid lines represent the cooling when the only coordinate is non-zero in the beginning and demonstrate full agreement with the theory.

[3] Following [2], we will treat these terms as dipole, quadrupole, and sextupole components, though actually each Bessel function generates all nonlinearities on the reference trajectory.

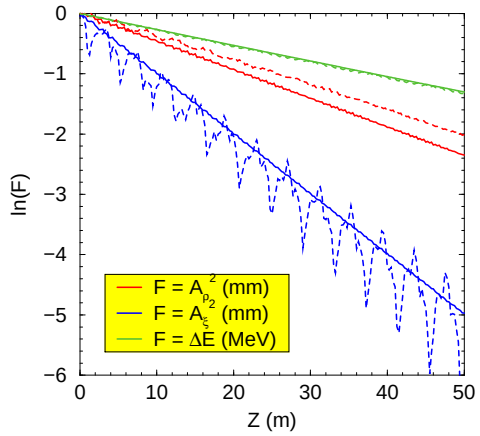

Figure 4: Single particle tracking at ionization cooling without stochastic effects. Dashed lines – all variables $\neq 0$ in the beginning, solid lines – only one of them $\neq 0$.

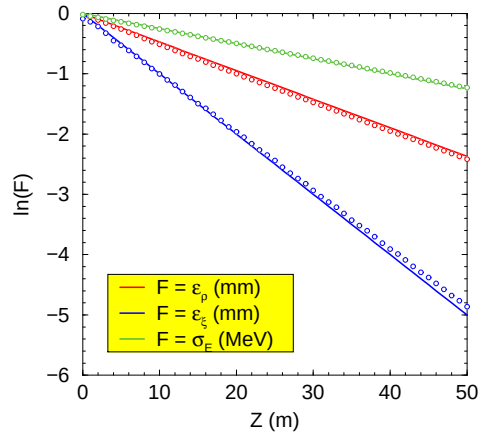

Figure 5: Cooling without stochastic effects. Solid lines – theory, circles – simulation of 1000 particles. Gaussian distribution in all degrees of freedom.

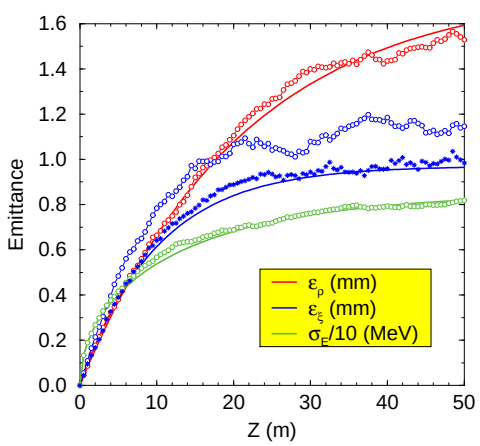

Figure 6: Cooling simulation of 1000 particles. Solid lines – theory, circles – simulation, stars – simulation without straggling.

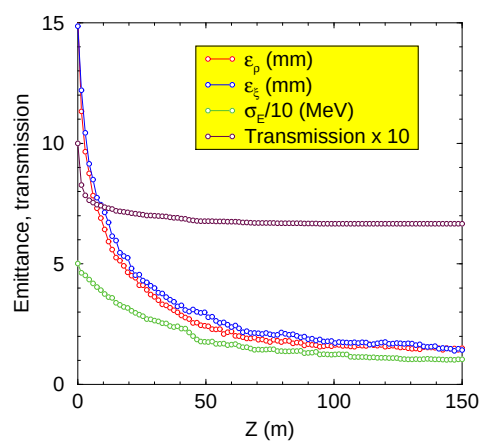

Figure 7: Cooling simulation of 1000 particles. Hydrogen absorber, ionization energy loss 17.3 MeV/m, straggling included.

More complicated case is when all the variables differ from 0 initially, a case which is presented in the graph by dashed lines. Because actually $G = 0$ at $\Delta E = 0$ only, there is transverse coupling at non-equilibrium energy which results in noticeable oscillations of azimuthal amplitude and some redistribution of transverse decrements. However, this effect is an odd function of energy deviation, which appears only slightly in the beam. The statement is confirmed by cooling simulation of 1000 particles which is presented in Fig. 5 together with theoretical data. In this case, the parasitic coupling causes only tiny little changes of the transverse decrements.

3.5 Cooling emittances

According to Eq. (33)–(35), equilibrium emittances should be in this case:

$$(\varepsilon_\rho)_{eq} = 1.8 \text{ mm}, \qquad (\varepsilon_\xi)_{eq} = 1.0 \text{ mm}, \qquad (\sigma_E)_{eq} = 8.6 \text{ MeV}\,.$$

Expected evolution of the beam at zero initial emittances is shown in Fig. 6 by solid lines. Results of simulation of 1000 particles are shown also by circles of the same color. Radial emittance and energy spread are in good agreement with theory, but azimuthal emittance is about 25% more. Most probably, this is the effect of coupling at non-equilibrium energy again, a statement which is confirmed by simulation at excluded straggling. Corresponding azimuthal emittance is presented by blue stars and much better meets the theory (the change of radial emittance is not shown because corresponding numerical and theoretical data are in full agreement, as before).

Cooling at non-zero initial emittances is demonstrated by Fig. 7 (straggling included). It is seen that both radial and azimuthal decrements are about the same in this case, a fact confirming parasitic transverse coupling. There is particle loss about 30% especially at very beginning, suggesting small acceptance of the channel [4] (a particle believed to be lost if its deviation exceeds $3\sigma_{initial}$ in any direction, no decay loss). However, final emittances are about the same as in Fig. 6.

[4]The loss is about 50% without sextupole correction

4 Helical Cooling Channel with linear coupling (Yonehara design)

The principal drawback of the coupling-free channel is very uneven distribution of decrements on degrees of freedom, because only radial oscillations are involved into the emittance exchange. Transverse coupling should be used to involve both transverse modes and to reach more uniform distribution. A suitable design proposed by K. Yonehara [3] is analyzed below. In terms of this paper, its main parameters are:

$$\kappa = 2\pi/\text{ m}, \quad p_0 = 250 \text{ MeV/c}, \quad X_0 = 1, \quad G_0 = 0.1189, \quad G_0' = 0.1236.$$

According to Eq. (8) and (11), main solenoid field is $B_0 = 6.96$ T in this case. Ionization energy loss is accepted as large as 14.7 MeV/m at the simulation. Other essential parameters will be presented at the analysis.

4.1 Field composition

Required parameters of the longitudinal field are: $F(1) = -0.234$, $F'(1) = -0.217$. They can be assured by 2-components field

$$B_1/B_0 = -0.5091, \qquad B_2/B_0 = 0.0777$$

which was proposed in Ref. [3] and is plotted in Fig. 8. The curve is more smooth in comparison with previous example (Fig. 1). Therefore, sextupole correction is not required now – a fact which is also noted in Ref. [3].

4.2 Dispersion and chromaticity

Normalized dispersion and eigentunes are plotted in Fig. 9 vs $\Delta p/p$. At $\Delta p/p = 0$, theoretical/numerical values are: $\nu_1 = 0.7423/0.7423$, $\nu_2 = 0.9150/0.9152$, $\kappa D = 1.768/1.767$. The dispersion function is about 2 times bigger now then in Fig. 2, a property which provides more intense emittance exchange and higher longitudinal damping.

4.3 Phase trajectories

Transverse phase trajectories are plotted in Fig. 10 at central momentum. Variables C_i and S_i defined by Eq. (19)–(20) are presented there, and Eq. (36)

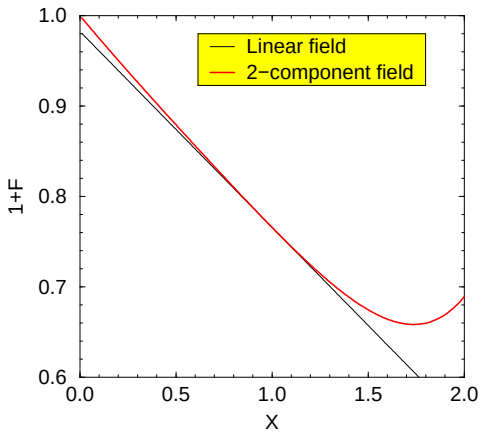

Figure 8: Two-component normalized longitudinal field on the reference trajectory. Linear field $1 + F = 0.766 - 0.217(X - 1)$ is shown for comparison.

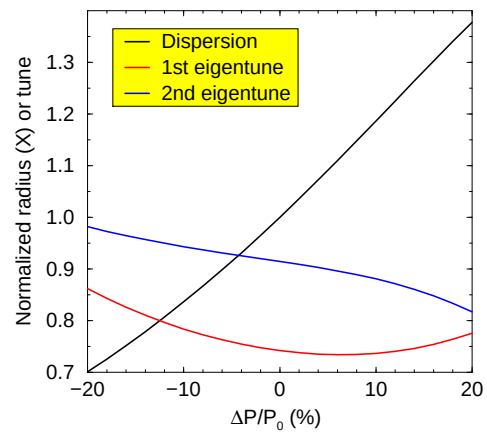

Figure 9: Dispersion and tunes vs relative particle momentum at the composed field. Tracking/theory difference does not exceeds 0.02% at $\Delta p/p = 0$.

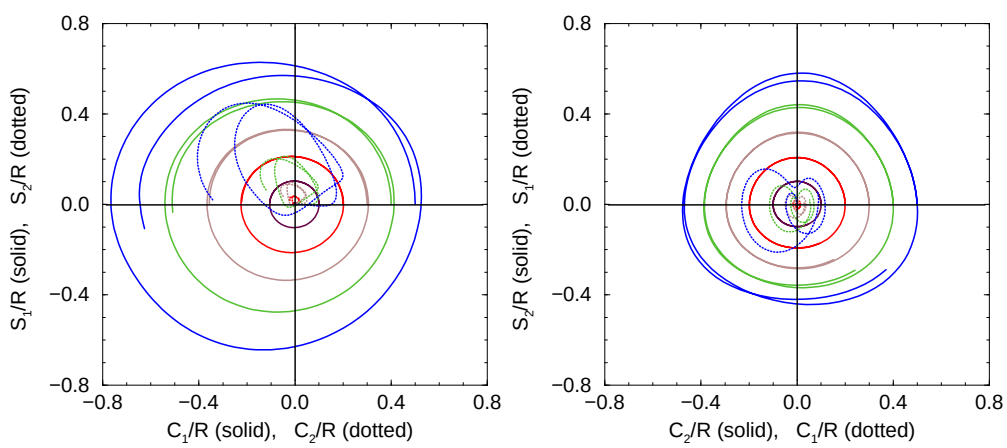

Figure 10: Phase trajectories of transverse motion. Variables C_i and S_i defined by Eq. (19)–(20) are plotted. Only first eigenmode is initially excited in the left-hand graph (solid lines), but second mode appears later due to parasitic coupling (dotted lines). Opposite case is considered in the right-hand plot.

is used to tie them to cylindrical coordinates. In full agreement with Eq. (19)–(22), the modes are uncoupled at small amplitudes, and corresponding beta-functions are: $\beta_1 = 28.0$ cm and $\beta_2 = 23.3$ cm. However, the coupling and other nonlinear effects appear at more amplitudes resulting in distortions of the trajectories. It allows to estimate the channel aperture as about $0.4/\kappa \sim$ 7 cm.

4.4 Cooling decrements

In this case, solution of Eq. (25)–(27) results in almost equal decrements of the cooling:

$$\lambda_1 = 0.552, \qquad \lambda_2 = 0.564, \qquad \lambda_E = 0.581\,.$$

Therefore, at ionization energy loss 14.7 MeV/m, characteristic cooling length Δz should be 20.0 m for 1st transverse mode, 19.6 m for 2nd mode, and 19.0 m for energy. Results of tracking and cooling simulation without stochastic effects are presented in Fig. 11 and 12 at the same format as in Fig. 4 and 5. The amplitudes and emittances of eigenmodes are calculated by Eq. (19)–(21). Corresponding decrements differ from theoretical values not more then by 2%.

4.5 Cooling emittances

According to Eq. (33)–(35), equilibrium emittances should be in this case:

$$(\varepsilon_1)_{eq} = 2.0 \text{ mm}, \qquad (\varepsilon_2)_{eq} = 1.4 \text{ mm}, \qquad (\sigma_E)_{eq} = 5.2 \text{ MeV}\,.$$

Simulation at zero initial conditions presented in Fig. 13 together with theoretical curves. Emittance of 2nd transverse mode is distinctly higher of the expected theoretical value (blue line). A possible explanation is that used theoretical eigenmodes are particularly true for reference energy and not fully adequate if energy spread is present. It can be added in support that the difference becomes less and does not exceed statistical error if the spread is kept small by excluding of straggling.

Cooling simulation at non-zero initial emittances is presented in Fig. 14. In this case, final emittances are almost the same as before though particles loss about 20% is observed in very beginning, and energy spread of the beam rapidly decreases at the same time. This allows to think that an excessive energy spread of injected beam is the main reason of the loss, and acceptable rms energy spread is about 40 MeV in this channel.

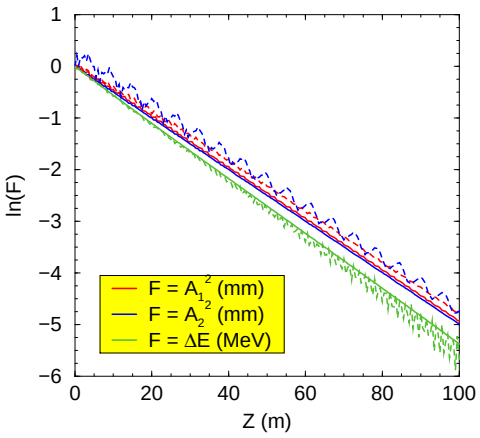

Figure 11: Single particle tracking at ionization cooling without stochastic effects. Dashed lines – all variables $\neq 0$ in the beginning, solid – only one of them $\neq 0$.

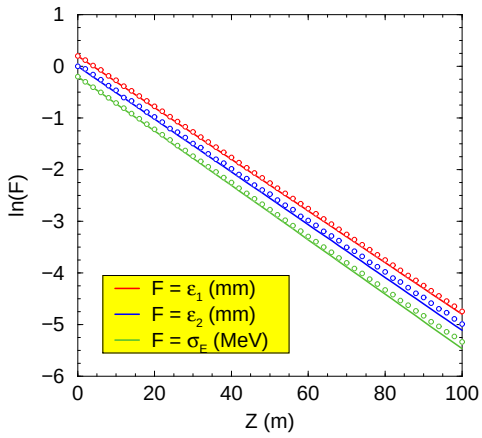

Figure 12: Cooling without stochastic effects. Solid lines – theory, circles – simulation of 1000 particles. Gaussian distribution in all degrees of freedom.

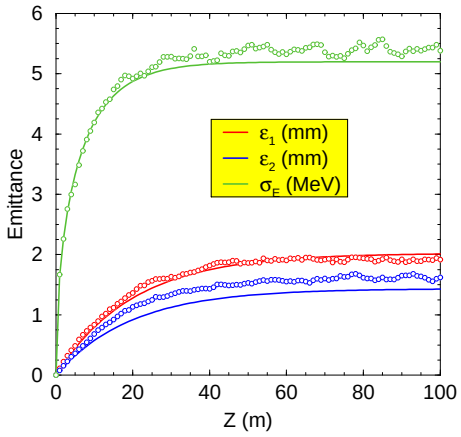

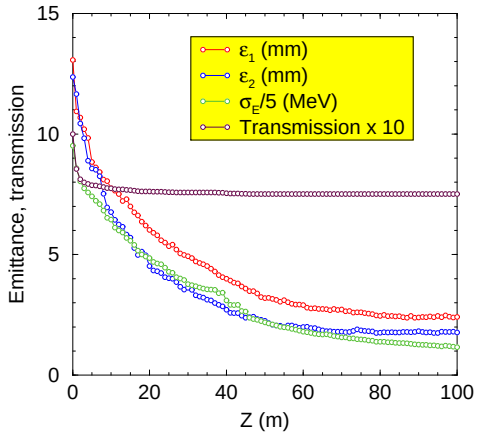

Figure 13: Circles – cooling simulation of 1000 particles at different initial conditions. Hydrogen absorber, energy loss 14.7 MeV/m. Solid lines – theory.

5 Shorter period channel

Beta-functions of the HCC should be proportional to its period which is the only fundamental length-dimensional parameter. [5] This allows to believe that equilibrium transverse emittance of cooled beam is about proportional to the period. To check this statement, we consider the same channel as in Sec. 4, but with twice shorter period (0.5 m instead of 1 m, solenoidal field 13.9 T at momentum 250 MeV/c). Results of the simulation presented in Fig. 14 affirm the statement as a whole. However, comparison with Fig. 13 reveals that discrepancy with the theory is more at shorter period. An effect of energy spread (which varies only slightly in these cases) is one of the reasons. An additional investigation has demonstrated that average transverse emittance coincides with theoretical value if the spread is kept small by excluding of straggling. However, difference of the emittances is still less by factor about 5 in comparison with the theory, probably because of nonlinear coupling which is another cause of the discrepancy. It is necessary to emphasize that dynamic aperture of the channel is proportional to the period length as well, and initial beam emittance should be decreased to avoid an excessive particle loss.

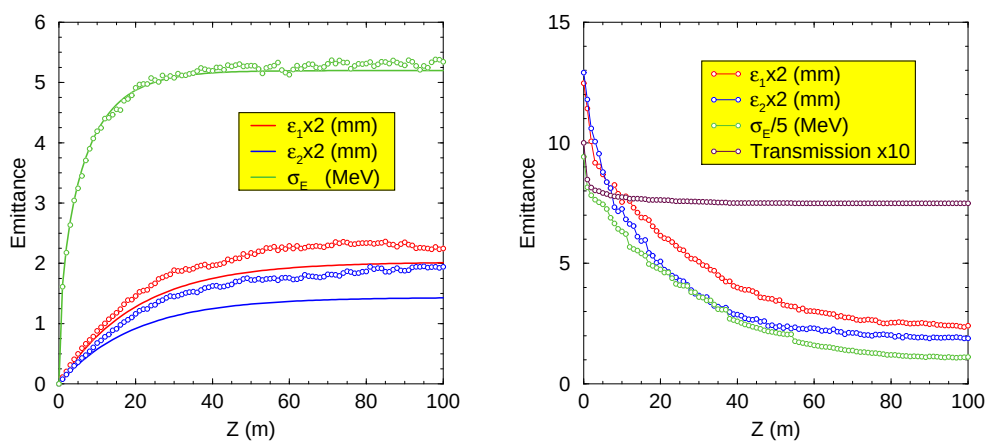

Figure 14: Cooling simulation of 1000 particles at different initial emittances. The same conditions as in Sec. 4, Fig. 13 except of period length.

[5] Cooling length is independent parameter, but it is not so important because force of the ionization friction is relatively small in practice. Role of wavelength at RF acceleration will be considered later.

6 Lower energy

Beam momentum was rather high in previous examples, requiring large solenoid field and resulting in large energy spread due to straggling. Therefore, a decrease of the momentum looks as a reasonable way to improve HCC characteristics. A channel of period 1 m at $p = 183$ MeV/c is considered in this section as an example. Its parameters are taken to provide uniform distribution of the cooling decrements:

$$X_0 = 1, \quad G_0 = 0.1835, \quad G_0' = 0, \quad B_0 = 4.92 \text{ T}, \quad E_i = 11.2 \text{ MeV/m}.$$

Then $\lambda_1 = \lambda_2 = \lambda_E = 0.5$, any partial cooling length $\Delta z = 20$ m, and normalized equilibrium emittances are:

$$(\varepsilon_1)_{eq} = 2.1 \text{ mm}, \qquad (\varepsilon_2)_{eq} = 1.5 \text{ mm}, \qquad (\sigma_E)_{eq} = 3.5 \text{ MeV}.$$

Following set of coefficients is used to generate the helical field:

$$B_1/B_0 = -0.4722, \qquad B_2/B_0 = 0.0653, \qquad B_3/B_0 = -0.0030$$

Results of the simulation are presented in Fig. 15 which should be compared with Fig. 13. As it was expected, behavior and value of transverse emittances are about the same, whereas final energy spread is reduced on about 30%. However, the channel acceptance falls even more, compelling to decrease initial emittances about 1.5 times to avoid an extensive particle loss. As a result, merit factor decreases almost 2 times in comparison with higher energy design.

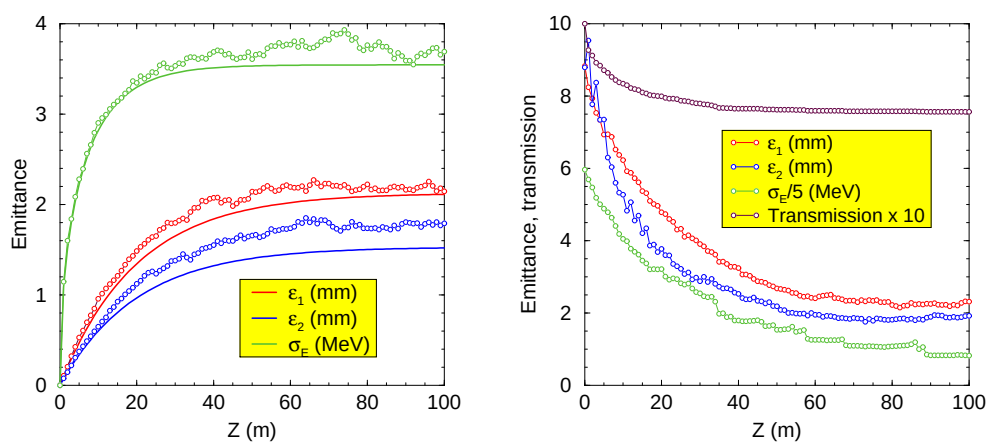

Figure 15: Circles – cooling simulation of 1000 particles, solid lines – theory. Hydrogen absorber, ionization energy loss 11.2 MeV/m.

7 Lower radius

HCC of less radius is considered in this section at beam momentum 183 MeV/c and period length 1 m. Its other parameters are:

$$X_0 = 0.625, \quad G_0 = 0.3192, \quad G_0' = 0, \quad B_0 = 5.46 \text{ T}, \quad E_i = 13.4 \text{ MeV/m}.$$

This set provides the same cooling decrements as before: $\lambda = 0.5$, $\Delta Z = 20$ m. The following field coefficients are used at the simulation:

$$B_1/B_0 = -0.1918, \qquad B_2/B_0 = -0.3095, \qquad B_3/B_0 = 0.1$$

The results are presented in Fig. 16. Though the attained emittances are less than in previous example (Fig. 15), two peculiarities should be noted. Firstly, the discrepancy between the simulation and linear theory is more now. In particular, one can conclude from the left-hand plot that emittance exchange strongly falls off at $z >\sim 20$ m (or at $\sigma_E >\sim 3$ MeV). Secondly, acceptance of the channel drops drastically at less radius resulting in more particles loss at the same initial emittances (right-hand plots). Probably, nonlinear effects form the basis of these discrepancies. This is confirmed by Fig. 17 where transverse phase space is presented in the same format as in Fig. 10. It follows from the comparison that dynamic aperture of the low-

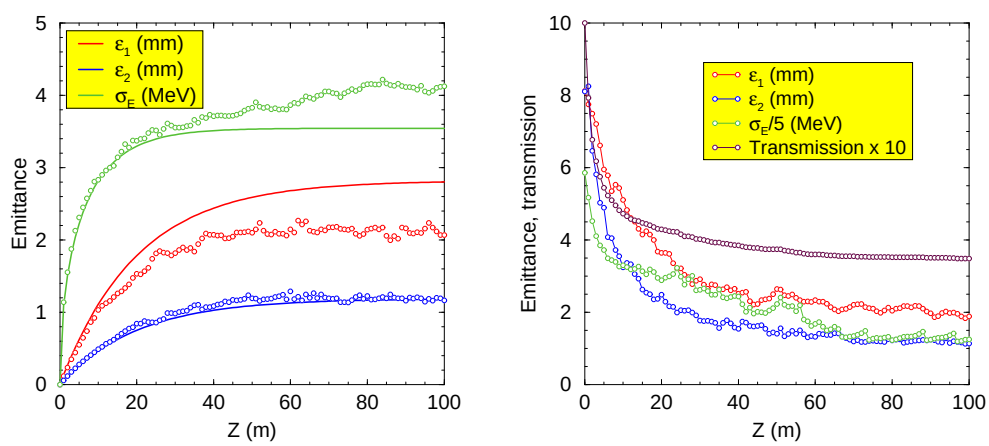

Figure 16: The same as in Fig. 15 at less helix radius: $X_0 = 0.625$ instead of 1. Energy loss 13.4 MeV/m is taken to have the same cooling length $\Delta z = 20$ m.

radius channel is at least twice less. Therefore, a noticeable excursion of X^2 from 1 looks unreasonably.

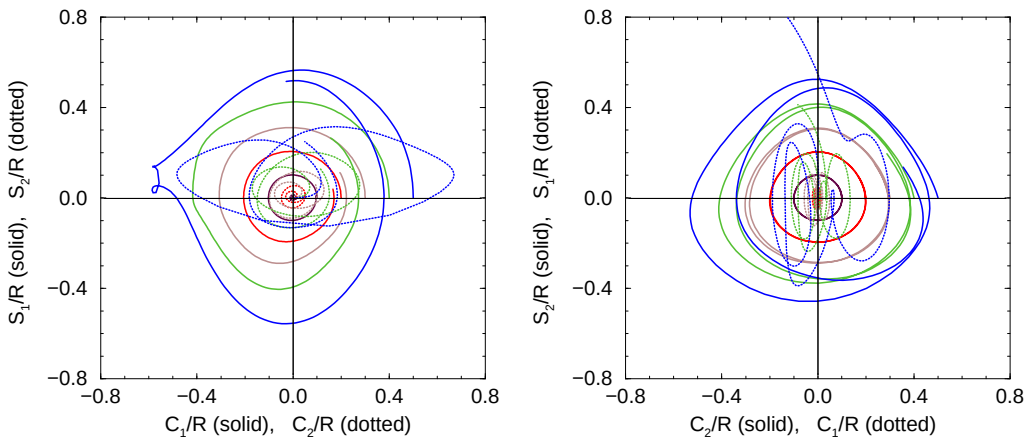

Figure 17: Phase trajectories of transverse motion. Variables C_i and S_i defined by Eq. (19)–(20) are plotted. Only first eigenmode is initially excited in the left-hand graph (solid lines), but second mode appears later due to parasitic coupling (dotted lines). Opposite case in the right-hand plot.

8 RF acceleration

Peculiarities produced by RF acceleration are discussed in this section. Because an engineering design is not a goal of this consideration, we will use traveling wave approximation at frequency f. Then acceleration field (24) has to be changed on

$$\vec{F}_a = \frac{E_{i0}\,\vec{a}}{\sqrt{1+X_0^2}} \Rightarrow \frac{E_{i0}\vec{a}}{\sqrt{1+X_0^2}}\,(\cos\phi - S\sin\phi), \qquad S = \sqrt{\frac{(eV')^2}{E_{i0}^2} - 1} \quad (37)$$

where V' is accelerating voltage per unit of length, $\phi = 2\pi f \Delta t$ – phase deviation of considered particle from reference one. As a result, Eq. (25) for energy obtains the form:

$$\frac{d\Delta E}{dz} = \frac{2E_i\sqrt{1+X^2}}{E\beta^2\gamma^2}\,\Delta E - \frac{E_i X \kappa \rho}{\sqrt{1+X^2}} - E_i S\sqrt{1+X^2}\,\phi \quad (38)$$

where assumption (30) is used and subindex '0' is omitted. It is easy to show that the phase satisfies the equation:

$$\frac{d\phi}{dz} = \frac{2\pi f}{v}\Big(\frac{X\kappa\rho}{\sqrt{1+X^2}} + \frac{Xd\xi}{dz} - \frac{\sqrt{1+X^2}}{\beta^2\gamma^2}\frac{\Delta E}{E}\Big) \tag{39}$$

Eq. (27) for azimuthal variable changes as well obtaining the form:

$$\frac{d^2\xi}{dz^2} + Q_\xi^2\kappa^2\xi = -\frac{\kappa G}{\sqrt{1+X^2}}\frac{d\rho}{dz} - \frac{E_i}{\beta^2 E}\Big(\sqrt{1+X^2}\frac{d\xi}{dz} - 2\kappa\rho - \frac{dE_i}{dE}\frac{X\Delta E}{E_i} - SX\phi\Big) \tag{40}$$

8.1 Synchrotron oscillations

The cooling channel considered in Sec. 4 is taken below for the numerical investigation at $f = 200$ MHz, $eV' = 2E_i = 29.5$ MeV/m. Other parameters are the same as in Sec. 4.

At commonly used approximation of uncoupled synchrotron and betatron oscillations, the values

$$\rho = \frac{D\Delta E}{\beta^2 E}, \qquad \xi = -\frac{dE_i}{dE}\frac{R^2\Delta E}{XQ_\xi^2\beta^2 E}$$

have to be substituted to Eq. (38)–(39) resulting in

$$\frac{d\Delta E}{dz} = -E_i S\sqrt{1+X^2}\,\phi + \Big(\frac{\kappa DX}{1+X^2} - \frac{2}{\gamma^2}\Big)\frac{E_i\sqrt{1+X^2}\Delta E}{\beta^2 E},$$
$$\frac{d\phi}{dz} = \frac{2\pi f}{\beta^2 E}\Big[\Big(\frac{\kappa DX}{\sqrt{1+X^2}} - \frac{\sqrt{1+X^2}}{\gamma^2}\Big)\Delta E + \frac{2E_i R^2}{\beta^2\gamma^2 E Q_\xi^2}\frac{d\Delta E}{dz}\Big]$$

Related phase trajectories are shown in left-hand Fig. 18 According it, parameters of small synchrotron oscillations are:

$$\text{Period length} \quad \Delta z = 7.3\ \text{m}, \quad \text{“Beta function”} \quad \hat{\beta}_E = \frac{\Delta(ct)}{\Delta E} = 0.57\,\frac{\text{cm}}{\text{MeV}}$$

at theoretical values 7.31 m and 0.568 cm/MeV. However, betatron oscillation strongly interfere in the picture. The statement is illustrated by right-hand Fig. 18 which is obtained by solution of full set of equations at $\rho_{init} = 2$ cm (typical betatron amplitude near statistical equilibrium). One can expect that observed jitter of the traces will result in noticeable increase of the synchrotron emittance.

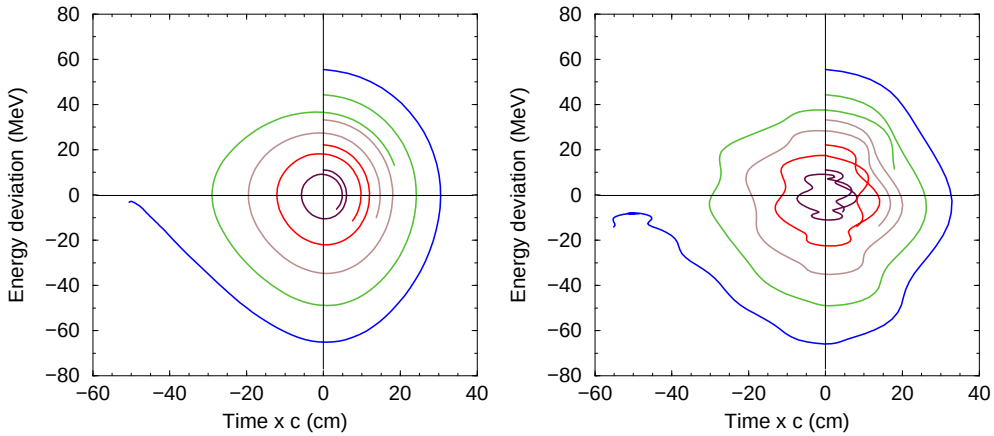

Figure 18: Phase plane of synchrotron oscillations. Left/right graphs – without/with betatron oscillations taken into account.

8.2 Cooling decrements

At the RF regime, cooling decrements are comparable with synchrotron frequency and somewhat differ from the "induction" ones:

$$\lambda_1 = 0.677, \qquad \lambda_2 = 0.491, \qquad \lambda_E = 0.529\,.$$

Corresponding effective damping lengths are:

$$\Delta z_1 = 16.6 \text{ m}, \qquad \Delta z_2 = 22.5 \text{ m}, \qquad \Delta z_E = 20.1 \text{ m}$$

Tracking and simulation without stochastic effects are presented in Fig. 19–20. Squares of amplitudes of a single particle are shown in Fig. 19 at the same format as in Fig. 11. At zero betatron amplitudes, behavior of the amplitudes is in good agreement with theory (solid lines). However, the synchrotron amplitude is very modulated at non-zero betatron amplitudes coinciding with the theory in average only. It cannot be doubted that the dependence of phase ϕ on transverse coordinates is a reason of the modulation. It almost disappears at an averaging on large number of particles as it is seen in Fig. 20, where cooling simulation of 1000 particles is presented. Calculated decrements are very close to theoretical ones, too.

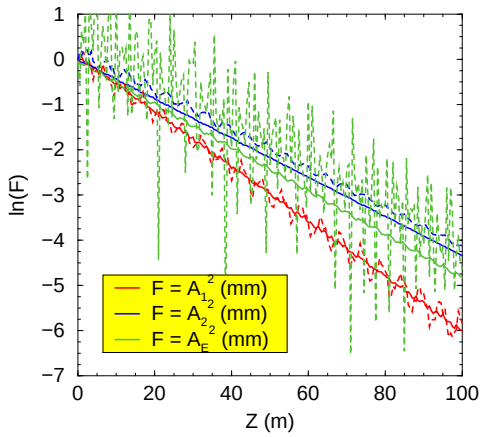

Figure 19: Single particle tracking at ionization cooling without stochastic effects. Dashed lines – all variables $\neq 0$ in the beginning, solid – only one of them $\neq 0$.

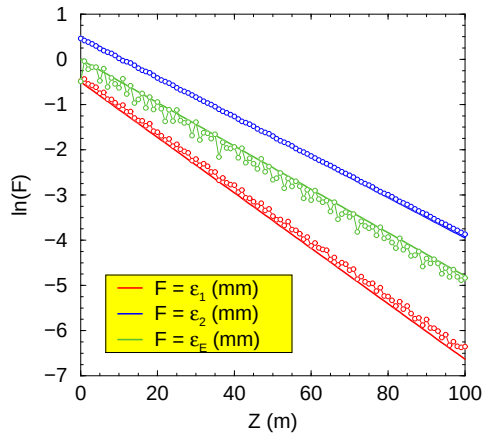

Figure 20: Circles – cooling simulation without stochastic effects. 1000 particles, Gaussian distribution in all degrees of freedom. Solid lines – theory.

8.3 Cooling emittances

Transverse equilibrium emittances are determined by Eq. (33) as before, and similar expression should be used for synchrotron emittance instead of Eq. (34):

$$(\varepsilon_E)_{eq} = \frac{\hat{\beta}_E \sigma_E^2}{mc^2} = \frac{\hat{\beta}_E E \beta^4 (\gamma^2 + 1)}{2\lambda_E} C_{str}$$

At $C_{sct} = 6.9 \times 10^{-3}$, $C_{str} = 2 \times 10^{-4}$, and $\beta_E = 0.57$ cm/MeV, calculation gives about equal emittances:

$$\epsilon_1 \simeq \epsilon_2 \simeq \epsilon_E \simeq 1.65 \text{ mm}.$$

Results of simulation and some theoretical curves are presented in Fig. 21. It is seen that transverse emittances exceed the theoretical values by $\sim 20\%$ that is about as at "induction" acceleration (and for the same reasons, see Sec. 4). Synchrotron emittance exceeds theoretical one significantly more – by factor 1.7 – 1.8. This is not particularly surprising because of perturbation caused by transverse motion and shown in Fig. 18. It follows from these figures as well, that rms energy spread and emittance cannot exceed about

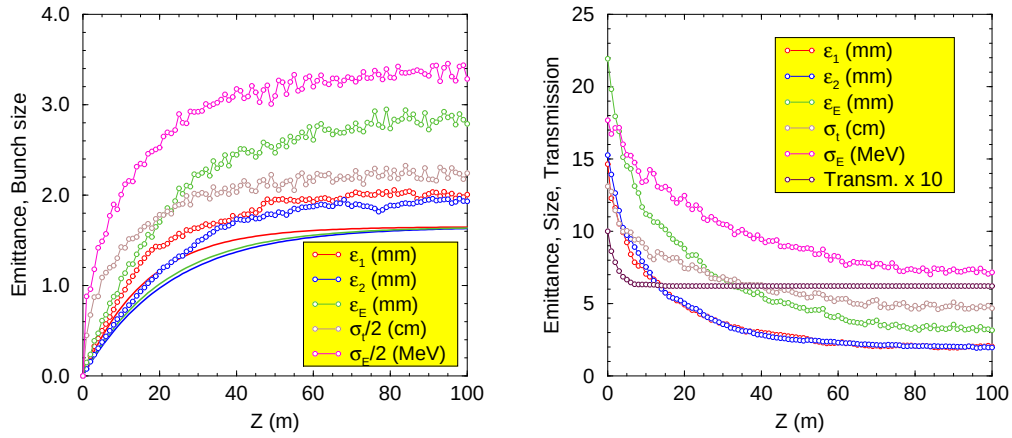

Figure 21: Circles – cooling simulation of 1000 particles at different initial conditions. Solid lines – theoretical emittances.

30 MeV and 40 mm, if particles fill the separatrix at constant phase density. Approximately 18 MeV/22 mm truncated Gaussian beam was used for cooling simulation presented in right-hand Fig. 21, causing 40% particles loss just after injection. About double diminution of the parameters looks reasonably because of mentioned difference of distributions and perturbations of synchrotron oscillations. Nevertheless, it should be noted that almost 3 times more rms energy spread is acceptable at the "induction" acceleration (see Fig. 13).

More detailed analysis of these problems and RF optimization requires additional investigations which are not an object of this work.

9 Conclusion

• Reasonable momentum range of the Helical Cooling Channel is $p = 200 - -250$ MeV/c. More momentum requires more magnetic field and leads to more energy spread and 6D emittance. Less momentum allows to decrease these parameters; however, the channel acceptance falls even faster, which circumstance requires to lower injected emittance and leads to dilution of merit factor.

• Optimal helix radius is about $L/2\pi$ where L is period length of the channel. Enlargement of the radius causes growth of transverse beta-functions and emittances, its reduction results in degradation of the channel acceptance.

• Homogeneous distribution of the cooling decrements on degrees of freedom creates nearly optimal cooling conditions and requires rather strong coupling of radial and azimuthal betatron oscillations.
• With hydrogen absorber, achievable transverse emittance is $(1.8\text{–}2)\times 10^{-3} L$ that is 1–2 mm at L =0.5–1 m.
• At optimal design, betatron acceptance exceeds the equilibrium emittance by factor 6–8 at reasonable particles loss.
• Required solenoid field is

$$B\,(\mathrm{T}) \simeq 0.03\,\frac{pc\,(\mathrm{MeV})}{L\,(\mathrm{m})}$$

that is 6–7 T at $L = 1$ m and 25–30 T at $L = 24$ cm. Helical field is about 4–5 times less on the reference helix. It depends on radius and certainly more on the coils; however, it is an engineering problem which is beyond the scope of this work.
• Energy spread 4–6 MeV is achievable at integrated ("inductive") accelerating. However, significant degradation is observed at FR acceleration, probably because of dependence of the RF phase on transverse coordinates and momenta. The problem requires an addition investigation.

10 Acknowledgments

Author thank K. Yonehara for an additional information about his design, S. Striganov for improved muon scattering data, and Y. Alexahin for general discussion.

References

[1] Y. Derbenev, http://www-mucool.fnal.gov/mcnotes/public/ps/muc0108 /muc0108.ps.gz (2000).

[2] Y. Derbenev and R. Johnson, Phys.Rev. ST-AB, 8, 041002 (2005).

[3] K. Yonehara et al., Proc. 2005 PAC, p. 3215, Knoxwill (2005).

[4] K. Yonehara, http://muonsinc.com/mcwfeb07/presentation/ Yonehara-021307.pdf (2007).